Defense Threat Reduction Agency
8725 John J. Kingman Road, MS-6201
Fort Belvoir, VA 22060-6201

DTRA-TR-22-026

TECHNICAL REPORT

Estimation of Inflammation and Repair Parameters for a Superficial Thermal Burn Model

October 2022

HDTRA1-14-D-0003

Prepared by:
Applied Research Associates, Inc.
801 N. Quincy Street
Suite 700
Arlington, VA 22203

UNIT CONVERSION TABLE

U.S. customary units to and from international units of measurement*

U.S. Customary Units	Multiply by → / ← Divide by†		International Units
Length/Area/Volume			
inch (in)	2.54	$\times 10^{-2}$	meter (m)
foot (ft)	3.048	$\times 10^{-1}$	meter (m)
yard (yd)	9.144	$\times 10^{-1}$	meter (m)
mile (mi, international)	1.609 344	$\times 10^{3}$	meter (m)
mile (nmi, nautical, U.S.)	1.852	$\times 10^{3}$	meter (m)
barn (b)	1	$\times 10^{-28}$	square meter (m^2)
gallon (gal, U.S. liquid)	3.785 412	$\times 10^{-3}$	cubic meter (m^3)
cubic foot (ft^3)	2.831 685	$\times 10^{-2}$	cubic meter (m^3)
Mass/Density			
pound (lb)	4.535 924	$\times 10^{-1}$	kilogram (kg)
atomic mass unit (AMU)	1.660 539	$\times 10^{-27}$	kilogram (kg)
pound-mass per cubic foot ($lb\ ft^{-3}$)	1.601 846	$\times 10^{1}$	kilogram per cubic meter ($kg\ m^{-3}$)
Pound-force (lbf avoirdupois)	4.448 222		Newton (N)
Energy/Work/Power			
electron volt (eV)	1.602 177	$\times 10^{-19}$	joule (J)
erg	1	$\times 10^{-7}$	joule (J)
kiloton (kT) (TNT equivalent)	4.184	$\times 10^{12}$	joule (J)
British thermal unit (Btu) (thermochemical)	1.054 350	$\times 10^{3}$	joule (J)
foot-pound-force (ft lbf)	1.355 818		joule (J)
calorie (cal) (thermochemical)	4.184		joule (J)
Pressure			
atmosphere (atm)	1.013 250	$\times 10^{5}$	pascal (Pa)
pound force per square inch (psi)	6.984 757	$\times 10^{3}$	pascal (Pa)
Temperature			
degree Fahrenheit (°F)	[T(°F) − 32]/1.8		degree Celsius (°C)
degree Fahrenheit (°F)	[T(°F) + 459.67]/1.8		kelvin (K)
Radiation			
activity of radionuclides [curie (Ci)]	3.7	$\times 10^{10}$	per second (s^{-1}‡)
air exposure [roentgen (R)]	2.579 760	$\times 10^{-4}$	coulomb per kilogram ($C\ kg^{-1}$)
absorbed dose (rad)	1	$\times 10^{-2}$	joule per kilogram ($J\ kg^{-1}$§)
equivalent and effective dose (rem)	1	$\times 10^{-2}$	joule per kilogram ($J\ kg^{-1}$**)

*Specific details regarding the implementation of SI units may be viewed at http://www.bipm.org/en/si/.

†Multiply the U.S. customary unit by the factor to get the international unit. Divide the international unit by the factor to get the U.S. customary unit.

‡The special name for the SI unit of the activity of a radionuclide is the becquerel (Bq). ($1\ Bq = 1\ s^{-1}$).

§The special name for the SI unit of absorbed dose is the gray (Gy). ($1\ Gy = 1\ J\ kg^{-1}$).

**The special name for the SI unit of equivalent and effective dose is the sievert (Sv). ($1\ Sv = 1\ J\ kg^{-1}$).

REPORT DOCUMENTATION PAGE

PLEASE DO NOT RETURN YOUR FORM TO THE ABOVE ORGANIZATION.

1. REPORT DATE	2. REPORT TYPE	3. DATES COVERED	
		START DATE	END DATE
10-19-2022	Technical Report		

4. TITLE AND SUBTITLE

Estimation of Inflammation and Repair Parameters for a Superficial Thermal Burn Model

5a. CONTRACT NUMBER	5b. GRANT NUMBER	5c. PROGRAM ELEMENT NUMBER
HDTRA1-14-D-0003		
5d. PROJECT NUMBER	**5e. TASK NUMBER**	**5f. WORK UNIT NUMBER**

6. AUTHOR(S)

Rachel Jennings, PhD, Amy Creel, Angela Reynolds, PhD

7. PERFORMING ORGANIZATION NAME(S) AND ADDRESS(ES)

Applied Research Associates, Inc.
801 N. Quincy Street, Suite 700
Arlington, VA 22203

8. PERFORMING ORGANIZATION REPORT NUMBER

9. SPONSORING/MONITORING AGENCY NAME(S) AND ADDRESS(ES)	10. SPONSOR/MONITOR'S ACRONYM(S)	11. SPONSOR/MONITOR'S REPORT NUMBER(S)
Defense Threat Reduction Agency - Nuclear Technologies Department, Attn: Dr. Blake 8725 John J. Kingman Road, Mail Stop 6201 Fort Belvoir, VA 22060-6201	DTRA-RD-NTS	DTRA-TR-22-026

12. DISTRIBUTION/AVAILABILITY STATEMENT

DISTRIBUTION A. Approved for public release: distribution is unlimited.

13. SUPPLEMENTARY NOTES

14. ABSTRACT

To study the local inflammatory response and early fibroblast activity initiated by a superficial thermal burn, a system of ordinary differential equations was formulated. The structural complexity of this TDPM, along with data limitations for nuclear detonation events, requires the identification of influential model parameters prior to parameter estimation, ensuring optimal calibration. Values for critical inflammation and repair parameters are derived and the model's behavior validated.

15. SUBJECT TERMS

Thermal Burn, Wound Healing, Inflammation, Modeling, Parameter Estimation, Calibration

16. SECURITY CLASSIFICATION OF:			17. LIMITATION OF ABSTRACT	18. NUMBER OF PAGES
a. REPORT	b. ABSTRACT	C. THIS PAGE		
U	U	U	U	32

19a. NAME OF RESPONSIBLE PERSON	19b. PHONE NUMBER *(Include area code)*
Paul K. Blake, PhD, GS-15	571.616.6117

PREVIOUS EDITION IS OBSOLETE.

STANDARD FORM 298 (REV. 5/2020)
Prescribed by ANSI Std. Z39.18

This page intentionally left blank.

Table of Contents

List of Figures

List of Tables

Acknowledgements

We gratefully acknowledge Dr. Paul Blake, Dr. Lawrence Herskowitz, and DTRA's Nuclear Technologies Survivability Division for programmatic support. This work was performed under DTRA contract HDTRA1-14-D-0003. We also thank external reviewers, Dr. Daniela Stricklin, LTC Lien Senchak, MD, Dr. David Schauer, and Dr. Aiguo Wu for their valuable feedback on the research presented in this technical report.

Executive Summary

To study the local inflammatory response and early fibroblast activity initiated by a superficial thermal burn, a system of ordinary differential equations was formulated. Despite being restricted to dynamics at the site of injury, the structural complexity of this model, along with data limitations for nuclear detonation events, requires the identification of influential model parameters prior to parameter estimation, ensuring optimal calibration. Here, values for critical inflammation and repair parameters- as determined by the results a prior global sensitivity analysis- are derived. Using the estimated values for these parameters, additional validation of the model is demonstrated by reproducing biological phenomena not imposed on the system. This is of importance given that the mathematical model will later serve as a foundational structure for the construction of physiologically driven models that not only adopt systems-level mechanistic frameworks but also leverage legacy models developed by the Defense Threat Reduction Agency to predict casualty distributions after a nuclear detonation event (i.e., those that have been implemented into the Health Effects from Nuclear and Radiological Environments tool, such as the granulopoiesis and lymphopoiesis models). Moreover, it will be used to obtain dynamic predictions of performance degradation and other downstream health outcomes.

Section 1. Introduction

Developed by Applied Research Associates (ARA) for the Defense Threat Reduction Agency (DTRA), the Health Effects from Nuclear Radiological Environments (HENRE) engine predicts casualties for the given environmental conditions following a nuclear detonation (NUDET) event. Current research efforts are focused on developing time-dependent physiological models (TDPMs) of injury resulting from combined insults. These models aim to expand HENRE's capabilities to dynamically predict outcomes essential to battlefield planning, such as performance decrement, and improve the human response models used in military doctrine.

Consisting primarily of ordinary differential equations (ODEs), the TDPMs developed for HENRE represent a subset of biological mathematical models that capture complex physiological processes in a mechanistic manner. Towards this goal, ARA has been developing a novel model that describes the immunological cascade following thermal radiation injury. This TDPM establishes the foundational basis for ongoing development of a computational model that fully captures the pathophysiology of combined injury resulting from human exposure to NUDET environments.

To obtain reliable model predictions, unknown parameters of these TDPMs must be estimated accurately. However, a lack of available data for NUDET events, along with the noisiness and temporal sparseness of the available data, adds further complexity to this already difficult task. Advances in parameter estimation methods present an opportunity to lessen the restraints imposed by these limitations and additionally strengthen the capability of the model's predictions. Traditional approaches to estimation of model parameters often use optimization algorithms, which produce a single value for unknown parameters; however, these approaches fail to explore the entire possible parameter space, do not account for uncertainty in the computed values, and are often vulnerable to overfitting.

To combat these shortcomings, brute-force with Latin-Hypercube sampling (LHS), which allows for parameters to varying across biologically feasible ranges, was applied to the TDPM for superficial thermal burns. This method the need for an idealized- but non-existent- dataset as parameter estimates were obtained by qualitatively matching the time series predictions produced by the model for varying point-wise parameter combinations to observed biological trends. Brute-force with LHS has been previously used in a model of wound healing (Cooper et al. 2015) and another describing pulmonary inflammation caused by mechanical ventilator-induced tissue damage (Minucci et al. 2021). In both instances, the authors selected this method not only due to the absence or impossibility of available experimental data, but also it accounted for population variability.

Section 2. Background

Thermal burns stem from absorption of thermal fluence by exposed skin, resulting in cell and tissue damage at varying depths; those that penetrate deeper levels of the skin are considered more severe (Evers et al. 2010). The physiological processes initiated by thermal burns- regardless of severity- follows the four phases of wound healing: hemostasis, inflammation, proliferation, and remodeling (Diegelmann and Evans 2004; Strudwick and Cowin 2018; Abazari et al. 2020). However, the modeling effort described therein focuses on superficial thermal burns, which is defined as superficial thickness (first-degree) and minor[1] partial thickness (second-degree) injuries in which timely healing occurs without scarring and intervention, and there is no or negligible risk of secondary infection (Evers et al. 2010; Wang 2014; Reeves 2018; Abazari et al. 2020; Jeschke et al. 2020).

It is worth highlighting that for thermal burns in military personnel, the face, neck, and hands are also the predominant injury location (Reeves 2018). By the Rule of Nines, the percent of total body surface area injured would be at most 13-19% (Wang 2014; Reeves 2018). For military personnel in the non-idealized (e.g., urban environment or where soldiers are in heavily armored vehicles), various structures will provide a considerable degree of shielding against thermal radiation, and this protection can also be enhanced by the uniforms of military personnel (Reeves 2018). Thus, these superficial thermal injuries align with prioritization on expanding HENRE's functionality to include temporal estimates of performance degradation as they are accompanied by varying degrees of pain (Vigani and Culler 2017; Lateef et al. 2019); noting that pain can occur for thermal injuries less severe than superficial thickness (first-degree).

Previously, to understand the "healthy" cascade, which corresponds to healing dynamics initiated by superficial thermal burns, a TDPM consisting of 23 ODEs was formulated (Jennings et al. 2022). This model aimed to capture hematopoietic and immunologic events across the bone marrow, lymphatic tissues, blood vessels, and local wound site. As superficial thermal injuries are assumed to not disrupt hematopoietic homeostasis (Hettiaratchy and Dziewulski 2004; Wang 2014), the model reduced to a subsystem of eight ODEs reflecting the innate and adaptive immune dynamics (inflammation phase) as well as early fibroblast activity (proliferation phase) at the injury site; that is, while hematopoietic dynamics are taken to be constant, they remain accounted for in the model, which describes localized inflammation and fibroblast activity in the wound itself. Inflammation served as the starting point for building a mechanistic model given its importance in healing outcomes. Fibroblast activity was included to indicate complete resolution of inflammation. Numerical simulations confirmed this localized model's ability to reproduce known and feasible biological behavior following superficial injury, thus establishing baseline healing dynamics for wounds arising from superficial thermal burn insults.

Although the TDPM was significantly reduced from its original form, it still contained 49 total parameters. The structural complexity of this model, along with the limited data available for NUDET events, risks introducing a considerable degree of uncertainty into model predictions. Therefore, prior to estimating the model's parameters, a global sensitivity analysis, which used Extended Fourier Amplitude Testing Sensitivity (eFAST), was performed to determine which parameters are most likely to contribute to prediction imprecision (Creel et al. 2022). The results of this analysis allowed for an

[1] Here, minor refers to less than 20% total body surface area (Jeschke et al. 2020).

informed decision to be made regarding which parameters could be fixed during the parameter estimation process. In this technical report, we continue the development of reduced TDPM by conducting parameter estimation for these critical parameters.

Section 3. Parameter Estimation

3.1 Time-Dependent Physiological Model

A TDPM of human immune response following superficial thermal burns was previously formulated by ARA (Jennings et al. 2022). In sum, the TDPM is comprised of 23 ODEs that mathematically describe immunological responses in the bone marrow, lymphatic tissue, blood vessels, and local thermal burn wound site that guide the inflammatory phase of healing following injury. Capturing these responses will be required when considering severe burns (e.g., second and third-degree and burns covering large amounts of the total body surface), which induce both local and systemic effects (Hettiaratchy and Dziewulski 2004; Wang 2014). However, while inflammatory mediators are also released at the superficial thermal burn site, this release does not spillover into circulation resulting in no systemic effects (Hettiaratchy and Dziewulski 2004; Wang 2014). Thus, it is assumed that hematopoietic dynamics remain constant following superficial injury and therefore the TDPM was reduced – via the quasi-steady state assumption – to eight ODEs consisting of 49 parameters. Here, only the reduced TDPM is considered, and the reader is referred to (Jennings et al. 2022) for a detailed discussion of the full and reduced model.

The system of ODEs describing the reduced TDPM satisfy

$$\begin{aligned}\frac{dDam_{tb}}{dt} = {} & k_{dn}\Omega_H(\Omega_i(N_{tb}; L2_{tb}, L2_2^{\infty}), 6, N_H) \\ & + \sigma_{dm1}k_{dn}\Omega_H(\Omega_i(M1_{tb}; L2_{tb}, L2_2^{\infty}), 6, M1_H) \\ & - \rho_{dam}\Omega_i(Dam_{tb}; Deb_{tb}, Deb_{dam}^{\infty}) - k_{df}F_{tb}\Omega_i(Dam_{tb}; Deb_{tb}, Deb_{dam}^{\infty})\end{aligned} \tag{1}$$

$$\begin{aligned}\frac{dDeb_{tb}}{dt} = {} & k_{dn}\Omega_H(\Omega_i(N_{tb}; L2_{tb}, L2_2^{\infty}), 6, N_H) \\ & + \sigma_{dm1}k_{dn}\Omega_H(\Omega_i(M1_{tb}; L2_{tb}, L2_2^{\infty}), 6, M1_H) \\ & - k_{dnp}N_{tb}\Omega_H(Deb_{tb}, 1, Deb_H) \\ & - k_{dm1p}\Omega_i(M1_{tb}; N_{tb}, N_1^{\infty})\Omega_H(Deb_{tb}, 1, Deb_H) \\ & - k_{dm2p}\Omega_i(M2_{tb}; N_{tb}, N_1^{\infty})\Omega_H(Deb_{tb}, 1, Deb_H) - d_{deb}Deb_{tb}\end{aligned} \tag{2}$$

$$\begin{aligned}\frac{dN_{tb}}{dt} = {} & \frac{s_{nr}R_n}{R_n + d_{nr}} - k_{nm1p}N_{tb}\Omega_i(M1_{tb}; N_{tb}, N_1^{\infty}) - k_{nm2p}N_{tb}\Omega_i(M2_{tb}; N_{tb}, N_1^{\infty}) \\ & - d_nN_{tb}\end{aligned} \tag{3}$$

$$\begin{aligned}\frac{dM1_{tb}}{dt} = {} & \frac{s_{mr}R_{m1}}{R_{m1} + R_{m2} + d_{mr}} - \theta_{m1m2}\left[k_{nm1p}N_{tb}\Omega_i(M1_{tb}; N_{tb}, N_1^{\infty})\right] + \theta_{m2m1}M2_{tb} \\ & - d_{m1}M1_{tb}\end{aligned} \tag{4}$$

$$\begin{aligned}\frac{dM2_{tb}}{dt} = {} & \frac{s_{mr}R_{m2}}{R_{m1} + R_{m2} + d_{mr}} + \theta_{m1m2}\left[k_{nm1p}N_{tb}\Omega_i(M1_{tb}; N_{tb}, N_1^{\infty})\right] - \theta_{m2m1}M2_{tb} \\ & - d_{m2}M2_{tb}\end{aligned} \tag{5}$$

$$\frac{dL1_{tb}}{dt} = \frac{s_{lr}k_{l1}\Omega_i(M1_{tb}; L2_{tb}, L2_1^{\infty})}{k_{l1}\Omega_i(M1_{tb}; L2_{tb}, L2_1^{\infty}) + k_{l2}\Omega_i(M2_{tb}; F_{tb}, F^{\infty}) + d_{lr}} - d_l L1_{tb} \tag{6}$$

$$\frac{dL2_{tb}}{dt} = \frac{s_{lr}k_{l2}\Omega_i(M2_{tb}; F_{tb}, F^{\infty})}{k_{l1}\Omega_i(M1_{tb}; L2_{tb}, L2_1^{\infty}) + k_{l2}\Omega_i(M2_{tb}; F_{tb}, F^{\infty}) + d_{lr}} - d_l L2_{tb} \tag{7}$$

$$\frac{dF_{tb}}{dt} = s_f + \Omega_i(F_{tb}; N_{tb}, N_2^{\infty}, M1_{tb}, M1_2^{\infty})\left(k_f + \alpha_{dam}Dam_{tb} + \alpha_{m2}M2_{tb}\right) - d_f F_{tb} \tag{8}$$

where

$$\Omega_i(X; Y_1, Y_1^{\infty}, \ldots, Y_m, Y_m^{\infty}) = \frac{X}{1 + \left(\frac{Y_1}{Y_1^{\infty}}\right)^2 + \ldots + \left(\frac{Y_m}{Y_m^{\infty}}\right)^2} \tag{9}$$

$$\Omega_H(X, n, X_H) = \frac{X^n}{X_H^n + X^n} \tag{10}$$

$$R_n = \Omega_i(k_{nd}Deb_{tb} + k_{nn}N_{tb}; M2_{tb}, M2^{\infty}, L2_{tb}, L2_1^{\infty}) \tag{11}$$

$$R_{m1} = \Omega_i(k_{m1d}Deb_{tb} + k_{m1n}N_{tb} + k_{m1m1}M1_{tb} + k_{m1l1}L1_{tb}; M2_{tb}, M2^{\infty}, L2_{tb}, L2_1^{\infty}) \tag{12}$$

$$R_{m2} = \Omega_i(k_{m2m1}M1_{tb} + k_{m2m2}M2 + k_{m2l2}L2; N_{tb}, N_1^{\infty}, M1_{tb}, M1_1^{\infty}, F_{tb}, F^{\infty}). \tag{13}$$

Descriptions of the model's state variables and assigned initial values used during parameter estimation are provided in Table 1. Observe from this table that two sets of initial conditions are considered to capture the two different types of superficial thermal burns of interest: one representing a superficial thickness burn (denoted as IC1), and the other a superficial partial thickness burn (denoted as IC2).

Table 1. Reduced TDPM (see Eqns. (1) – (13)) state variable symbols, definitions, and initial values.

SYMBOL	DESCRIPTION	INITIAL VALUE	
		Superficial Thickness (IC1)	Superficial Partial-Thickness (IC2)
t	Time (in hours)	-	-
Local Thermal Burn			
$\mathbf{Dam}_{tb}$	Damaged tissue (unitless)	0.1	0.9
$\boldsymbol{Deb}_{tb}$	Debris (unitless)	0.1	0.9
$\boldsymbol{N}_{tb}$	Activated neutrophils at the burn site	0	0
$\boldsymbol{M1}_{tb}$	Classically activated macrophages (M1) at the burn site	0	0
$\boldsymbol{M2}_{tb}$	Alternatively activated macrophages (M2) at the burn site	0	0
$\boldsymbol{L1}_{tb}$	Pro-inflammatory T lymphocytes, including $\gamma\delta$-T cells, TH1 cells, and TH17 cells, at the burn site	0	0
$\boldsymbol{L2}_{tb}$	Anti-inflammatory T lymphocytes, which includes TH2 cells, and regulatory T cells, at the burn site	0	0
$\boldsymbol{F}_{tb}$	Fibroblasts at the burn site	0	0

Figure 1 provides a schematic of the state variables and their relationships. State variables are represented using circles and squares. The solid black lines indicate transitions between different cellular states. Solid lines that feedback into the state variable itself indicate proliferation. Initiated cellular interactions are captured by dotted lines and remain locally concentrated. Blue and white colors are used to distinguish between up-regulatory (i.e., increasing in response to the cells themselves) and destructive/inhibitory relationships, respectively.

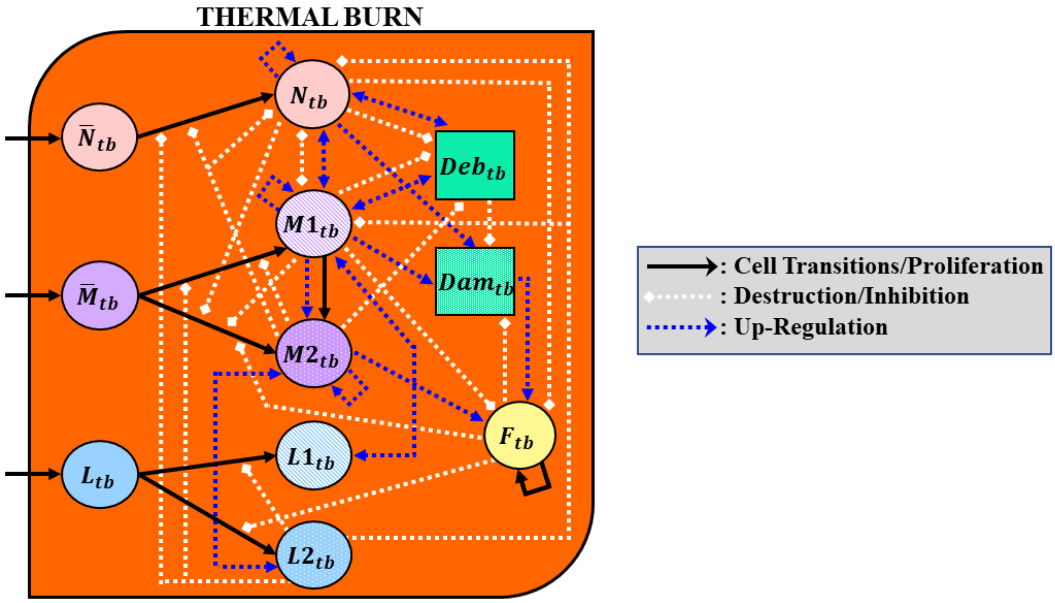

Figure 1. Schematic diagram of superficial thermal burn TDPM state variables, and their relationships.

3.2 Selected Parameters

In (Creel et al. 2022), eFAST, a method of global sensitivity analysis, was applied to all 49 parameters of the reduced TDPM. The results of eFAST allowed for delineation between those parameters having the least and greatest influence on model dynamics. It was determined that 27 parameters be estimated (see Table 2) while the other 22 parameters remain fixed at their baseline values (see Table 3); for a more in depth discussion on how these delineations were made, see (Creel et al. 2022). Note that descriptions of the parameters are also provided in both tables.

Table 2. Estimated parameter symbols, definitions, biological units, ranges, and representative set values.

PARAMETER		DESCRIPTION	UNITS	REPRESENATIVE SET	MINIMUM	MAXIMUM
Inhibition	Deb_H	Constant controlling the effectiveness of Deb_{tb} at inhibiting phagocytic removal of debris by N_{tb}, $M1_{tb}$, and $M2_{tb}$	D-units	0.0522	0.00042065	0.20176
	N_1^{∞}	Constant controlling the effectiveness of N_{tb} at inhibiting the activity of other immune cells	N-units	0.3870	0.0085501	0.75198
	$M1_1^{\infty}$	Constant controlling the effectiveness of $M1_{tb}$ at inhibiting activation of $M2_{tb}$	M-units	0.1681	0.012607	0.39033
	$M1_2^{\infty}$	Constant controlling the effectiveness of $M1_{tb}$ at inhibiting proliferation and activation of F_{tb}	M-units	0.0064	0.000026341	0.09559
	$M2^{\infty}$	Constant controlling the effectiveness of $M2_{tb}$ at inhibiting activation of N_{tb} and $M1_{tb}$	M-units	0.2280	0.0022269	0.50584
	$L2_1^{\infty}$	Constant controlling the effectiveness of $L2_{tb}$ at inhibiting the activation of N_{tb}, $M1_{tb}$, and $L1_{tb}$	L-units	0.1986	0.0014304	0.57992
Debris	k_{dnp}	Phagocytosis rate of Deb_{tb} by N_{tb}	D-units/(N-units·h)	0.0177	0.0000035432	0.022296
	k_{dm1p}	Phagocytosis rate of Deb_{tb} by $M1_{tb}$	D-units/(M-units·h)	0.0167	0.000062124	0.020856
	k_{dm2p}	Phagocytosis rate of Deb_{tb} by $M2_{tb}$	D-units/(M-units·h)	0.0034	0.000072101	0.01107
Neutrophils	s_{nr}	Recruitment rate of circulating neutrophils to the local burn site	N-units/h	1.4843	0.0000012566	0.11966
	k_{nd}	Activation rate of resting neutrophils to N_{tb} by Deb_{tb}	1/(D-units·h)	0.3165	0.000072334	0.58196
	d_{nr}	Decay rate of resting neutrophils	1/h	0.1524	0.00019076	0.16095

PARAMETER		DESCRIPTION	UNITS	REPRESENATIVE SET	MINIMUM	MAXIMUM
	d_n	Decay rate of N_{tb}	1/h	0.2512	0.00004281	0.29019
Macrophages	s_{mr}	Recruitment rate of tissue-resident macrophages and circulating monocytes to the local burn site	M-units/h	4.3038	0.048912	1.36375
	k_{m1d}	Activation rate of resting monocytes and tissue-resident macrophages to $M1_{tb}$ by Deb_{tb}	1/(D-units·h)	0.0101	0.000017763	0.013181
	k_{m1l1}	Activation rate of resting monocytes and tissue-resident macrophages to $M1_{tb}$ by $L1_{tb}$ and its byproducts	1/(L-units·h)	0.0003576	0.00000067238	0.0017841
	k_{m2m1}	Activation rate of resting monocytes and tissue-resident macrophages to $M2_{tb}$ by $M1_{tb}$ and its byproducts	1/(M-units·h)	0.0154	0.00004678	0.01887
	k_{m2l2}	Activation rate of resting monocytes and tissue-resident macrophages to $M2_{tb}$ by $L2_{tb}$ and its byproducts	1/(L-units·h)	0.0105	0.000013268	0.013324
	d_{mr}	Decay rate of resting monocytes and tissue-resident macrophages	1/h	0.0221	0.0000043242	0.036718
	d_{m1}	Decay rate of $M1_{tb}$	1/h	0.0582	0.005074	0.17882
	d_{m2}	Decay rate of $M2_{tb}$	1/h	0.1058	0.00033292	0.20059
	α_{m2}	Constant controlling the up-regulation of F_{tb} proliferation and activation by $M2_{tb}$	1/(M-units·h)	0.0315	0.0011855	0.046855
T Lymphocytes	$s_{\ell r}$	Recruitment rate of circulating T lymphocytes to the local burn site	L-units/h	0.0285	0.0030641	2.52021
	k_{l1}	Induction rate of activated (effector) T lymphocytes to $L1_{tb}$ by $M1_{tb}$	1/(M-units·h)	0.0978	0.0000002868	0.11898
	k_{l2}	Induction rate of activated (effector) T lymphocytes to $L2_{tb}$ by $M2_{tb}$	1/(M-units·h)	0.0057	0.00010587	0.015349

PARAMETER		DESCRIPTION	UNITS	REPRESENATIVE SET	MINIMUM	MAXIMUM
	$d_{\ell r}$	Decay rate of activated (effector) T lymphocytes	1/h	0.0620	0.000083327	0.11333
	d_{ℓ}	Decay rate of $L1_{tb}$ and $L2_{tb}$	1/h	0.1015	0.00036903	0.1190
Notation: h is hours, the timescale of the model. D represents the units for Dam_{tb} and Deb_{tb}, since it is the same for both. N, M, F, and L denote the units of neutrophils (N_{tb}), macrophages ($M1_{tb}$ and $M2_{tb}$), fibroblasts (F_{tb}), and T lymphocytes ($L1_{tb}$ and $L2_{tb}$), respectively.						

Table 3. Fixed parameter symbols, definitions, biological units, and assigned baseline values.

PARAMETER		DESCRIPTION	UNITS	BASELINE VALUE
Inhibition	Deb_{dam}^{∞}	Constant controlling the effectiveness of Deb_{tb} at inhibiting damage repair	D-units	0.01
	N_2^{∞}	Constant controlling the effectiveness of N_{tb} at inhibiting proliferation and activation of F_{tb}	N-units	0.1
	F^{∞}	Constant controlling the effectiveness of F_{tb} at inhibiting the activation of $M2_{tb}$ and $L2_{tb}$	F-units	0.53137
	$L2_2^{\infty}$	Constant controlling the effectiveness of $L2_{tb}$ at inhibiting collateral damage associated with N_{tb} and $M1_{tb}$	L-units	0.12
Damage and Debris	k_{dn}	Maximum collateral tissue damage rate caused by N_{tb} at the local burn site	D-units/h	0.000175
	σ_{dm1}	Tissue damage scaling coefficient for $M1_{tb}$	Unitless	0.5
	N_H	Hill constant for tissue damage associated with N_{tb}	N-units	0.06
	$M1_H$	Hill constant for tissue damage associated with $M1_{tb}$	M-units	0.06
	ρ_{dam}	Baseline tissue damage repair rate via a combination of repair, resolution, and regeneration	1/h	0.004
	k_{df}	Repair rate of Dam_{tb} by F_{tb}	1/(F-units·h)	0.02
	d_{deb}	Decay rate of Deb_{tb}	1/h	0.0001
Neutrophils	k_{nn}	Activation rate of resting neutrophils to N_{tb} by N_{tb} and its byproducts	1/(N-units·h)	0.0168611
	k_{nm1p}	Phagocytosis rate of N_{tb} by $M1_{tb}$	1/(M-units·h)	0.12075
	k_{nm2p}	Phagocytosis rate of N_{tb} by $M2_{tb}$	1/(M-units·h)	0.3628333
Mac	k_{m1n}	Activation rate of resting monocytes and tissue-resident macrophages to $M1_{tb}$ by N_{tb} and its byproducts	1/(N-units·h)	0.0034618

PARAMETER		DESCRIPTION	UNITS	BASELINE VALUE
	k_{m1m1}	Activation rate of resting monocytes and tissue-resident macrophages to $M1_{tb}$ by $M1_{tb}$ and its byproducts	1/(M-units·h)	0.000037879
	k_{m2m2}	Activation rate of resting monocytes and tissue-resident macrophages to $M2_{tb}$ by $M2_{tb}$ and its byproducts	1/(M-units·h)	0.00067667
	θ_{m1m2}	Transition rate of $M1_{tb}$ to $M2_{tb}$	M-units/N-units	0.6900833
Fibroblasts	s_f	Non-injury recruitment rate of fibroblasts to the local burn site	F-units/h	0.0013889
	d_f	Decay rate of F_{tb}	1/h	0.0090909
	k_f	Baseline proliferation and activation rate of F_{tb}	1/h	0.0053333
	α_{dam}	Constant controlling the up-regulation of F_{tb} proliferation and activation by Dam_{tb}	1/(D-units·h)	0.0666667

Notation: h is hours, the timescale of the model. D represents the units for Dam_{tb} and Deb_{tb}, since it is the same for both. N, M, F, and L denote the units of neutrophils (N_{tb}), macrophages ($M1_{tb}$ and $M2_{tb}$), fibroblasts (F_{tb}), and T lymphocytes ($L1_{tb}$ and $L2_{tb}$), respectively.

3.3 Brute-Force with Latin-Hypercube Sampling

As a type of Monte Carlo experiment, brute-force with LHS represents a qualitative method that uses the LHS algorithm to sweep the possible parameter space identifying point-wise parameter combinations that satisfy known qualitative biological trends (Cooper et al. 2015); this results in not a distribution, but a collection of discrete points, which is referred to as the *accepted set*. These pre-defined biological trends are extrapolated from the available data and then pooled together to form *acceptability criteria*. The brute-force differs from traditional curve fitting methods for parameter estimation because it involves finding combinations of parameters that qualitatively match pre-defined, known biological features, rather than a single parameter combination that maximizes the model's "goodness-of-fit" to experimental data. This method is advantageous in circumstances where experimental time series data of all the state variables (or a sufficient subset) are extremely limited or unavailable, but generalizations from the available data or existing literature can be made via pooling across different experiments. Hence, it is highly desirable for dealing with the TDPMs developed for HENRE due to data limitations for human subjects associated with NUDET research.

Brute-force relies on LHS, which exhaustively searches the possible parameter space, as an alternative to simple random sampling. McKay et al. first introduced LHS in 1979 as a stratified sampling without replacement technique, where predefined model parameter distributions are divided into *N* equiprobable intervals, allowing for sampling to then occur at the interval level (McKay et al. 1979; Marino et al. 2008). This method ensures efficient exploration of the full parameter space at a reduced computational cost (Blower and Dowlatabadi 1994).

3.3.1. Acceptability Criteria

Qualitative features that reflect the current knowledge of the biological system must be defined to determine plausible parameter combinations. These features were extracted either from the published literature or from available data directly. For each LHS-generated parameter combination, Eqns. (1)-(13) were numerically integrated over $t \in [0, 15 * 24]$ for IC1 and IC2. A wound is deemed as "healed" when $Dam_{tb} < 0.01$ (Lateef et al. 2019).

The acceptability criteria are summarized in Table 4.

Table 4. Acceptability criteria for parameter combinations prescribed under LHS.

CRITERIA	BIOLOGICAL DESCRIPTION	MATHEMATICAL REPRESENTATION	REFS.
AC1	Debris must be removed before damaged tissue can be repaired (follows from the definition of the inflammatory phase)	• $\tau_{deb} < \tau_{dam}$	(Goldberg and Diegelmann 2010; Schultz et al. 2011)
AC2	Superficial thickness and minor partial thickness burns heal within 3-6 days, and 7-21 days, respectively, without intervention	• For a superficial thickness burn (IC1), ▪ $3 \text{ days} \leq \tau_{dam} < 7 \text{ days}$ ▪ $\left\|\boldsymbol{X}_{IC1}^{tail} - \boldsymbol{X}^*\right\|_2 < 0.3$ ** • For a minor superficial partial thickness burn (IC2), ▪ $7 \text{ days} \leq \tau_{dam} \leq 14 \text{ days}$ ▪ $\left\|\boldsymbol{X}_{IC2}^{tail} - \boldsymbol{X}^*\right\|_2 < 0.3$ **	(Peng et al. 2006; Evers et al. 2010; Reeves 2018; Abazari et al. 2020; Jeschke et al. 2020)
AC3	Superficial burns heal without scarring	• $\left\|\boldsymbol{X}_{IC1}^{tail} - \boldsymbol{X}^*\right\|_2 < 0.3$ • $\left\|\boldsymbol{X}_{IC2}^{tail} - \boldsymbol{X}^*\right\|_2 < 0.3$	(Finnerty et al. 2016)

Notation: Let τ_{dam} and τ_{deb} be the time points such that $Dam(\tau_{dam}) < 0.01$ and $Deb(\tau_{deb}) < 0.01$, respectively.

** $\|\cdot\|_2$ represents the 2-norm of a matrix, which computes the maximum absolute row sum. $\boldsymbol{X}_{IC1}^{tail}$ and $\boldsymbol{X}_{IC2}^{tail}$ represent the "tail" numerical solution over $t \in [0, 100 * 24]$ (in hours) of all state variables under IC1 and IC2, respectively (see Table 1. The healed steady-state is that in which all state variables except fibroblasts are zero, i.e., $(Dam^*, Deb^*, N^*, M1^*, M2^*, F^*, L1^*, L2^*)^T = \left(0,0,0,0,0, \frac{s_f}{d_f - k_f}, 0,0\right)^T$ where T denotes the transpose of a matrix. Thus, $\boldsymbol{X}^*$ is taken to be $(Dam^*, Deb^*, N^*, M1^*, M2^*, L1^*, L2^*)^T$, whence $\left\|\boldsymbol{X}_{IC1}^{tail} - \boldsymbol{X}^*\right\|_2$ and $\left\|\boldsymbol{X}_{IC2}^{tail} - \boldsymbol{X}^*\right\|_2$.

3.3.2. Assigned Parameter Distributions and Sampling

To apply LHS, each estimated parameter must first be assigned a distribution. Here, 27 parameters are assumed to be uniformly distributed on a closed interval; note that the uniform distribution is recommended when the true distribution is unknown (Marino et al. 2008a). Table 2 lists the bounds for each parameter that will be approximated.

For the remaining three parameters (s_{nr}, s_{mr}, s_{lr}), random sampling constrained by certain stability criteria for the healed steady state[2] was applied. The stability criteria were analytically derived by finding the conditions under which all eigenvalues of the Jacobian evaluated at the healed steady-state will have negative real-parts, ensuring the healed steady-state is stable. Specifically, we require the following inequalities be satisfied:

1. $s_{nr} < \frac{d_{nr} d_n}{k_{nn}}$
2. $s_{mr} < \frac{d_{mr} d_{m1}}{k_{m1m1}}$

[2] The healed steady state, denoted as $(Dam_{tb}^*, Deb_{tb}^*, N_{tb}^*, M1_{tb}^*, M2_{tb}^*, F_{tb}^*, L1_{tb}^*, L2_{tb}^*)^t$ corresponds to all state variables being zero except fibroblasts, i.e., $Dam_{tb}^* = Deb_{tb}^* = N_{tb}^* = M1_{tb}^* = M2_{tb}^* = L1_{tb}^* = L2_{tb}^* = 0$, and $F_{tb}^* = \frac{s_f}{d_f - k_f}$. Observe that $F_{tb}^* > 0$ is always guaranteed since $d_f > k_f$ (see the assigned baselines for d_f and k_f in Table 3).

3. $s_{lr} < \frac{d_{lr} d_l (d_{mr} d_{m1} - s_{mr} k_{m1m1})}{s_{mr} k_{m1l1} s_{lr} k_{l1}}$

Note that the second inequality guarantees the difference on the right hand-side of the third inequality will always be positive. This was done to maximize the number of parameter combinations accepted. Using LHS and this constrained random sampling, 300,000 distinct parameter combinations were generated.

3.4 Representative Set

From the accepted parameter combinations, a representative set is derived; this set consists of a single, pointwise estimate assigned to each parameter such that the associated predicted model dynamics best correspond to the averaged behavior across all time points produced under the accepted parameter combinations. Following the approach in (Cooper et al. 2015), the mean at each time point across all accepted parameter combinations is computed for each state variable. These temporal means are used to compute the weighted mean sum squared error[3] of each accepted parameter combination for each state variable, and the resulting eight mean sum squared errors are then averaged. This process is performed on both initial condition sets. The representative set is then taken to be that parameter combination in the accepted set whose sum of average mean sum squared error for both initial conditions is smallest.

Brute-force with LHS applied to the superficial thermal burn model was implemented in MATLAB (2020).

[3] Let y denote a state variable of the model. Here, weighted mean sum squared error is defined as

$$\frac{1}{N_T}\left(\sum_{i=1}^{N_T} \frac{\left[y_j(t_i) - y_{mean}(t_i)\right]^2}{\sigma_i^2}\right)$$

where N_T is the total number of time points; $y_j(t_i)$ is the model predicted value at time point t_i under the jth parameter combination; $y_{mean}(t_i)$ is the mean of y at time point t_i across all parameter combinations in the accepted set; and σ_i^2 is the variance at y at time point t_i across all parameter combinations in the accepted set.

Section 4. Results

4.1 Accepted Parameter Combinations

Of the 300,000 parameter combinations generated, 1,298 satisfied the acceptability criteria listed in Table 4. Figure 1 thru Figure 8 display individual half-violin and half-histogram plots for each of the estimated parameters; these plots were constructed in MATLAB using the supplementary code of Bechtold (Bechtold 2016). In each plot, the y-axis denotes the values for that parameter whose units can be found in Table 3.The left-hand side represents a traditional violin plot with the features of a boxplot, such as the interquartile range and median, highlighted by the darker shaded region/line. An open circle marks the value of the corresponding mean. The right-hand side is a histogram of the same point-wise parameter estimates, providing an additional visualization of a parameter's distribution.

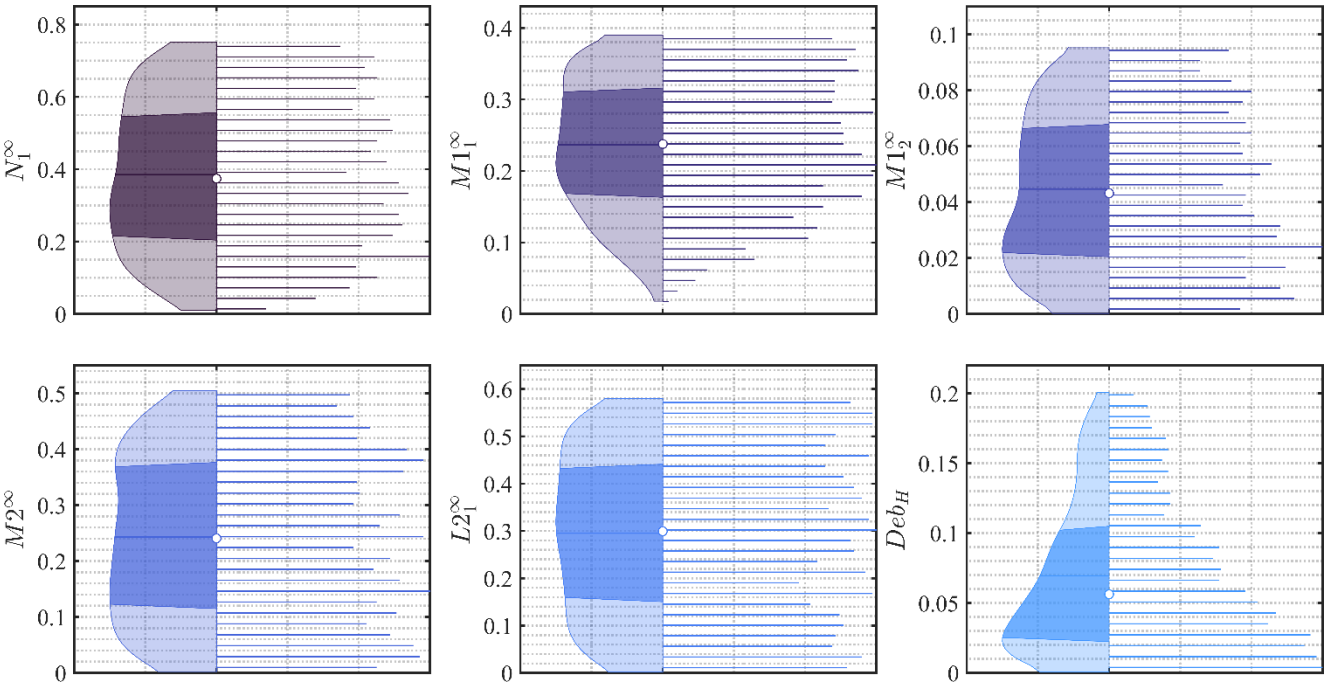

Figure 2. Half-violin plots for the estimated inhibition parameters.

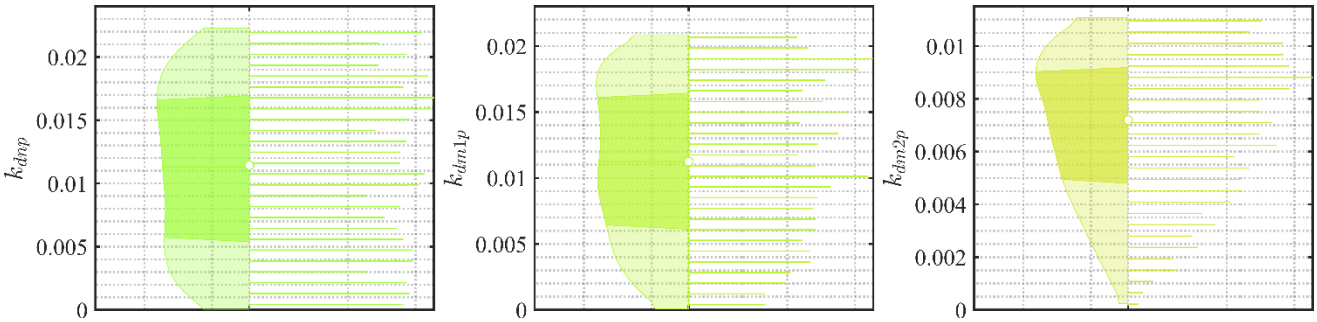

Figure 3. Half-violin plots for the estimated parameters describing phagocytosis of debris at the wound site.

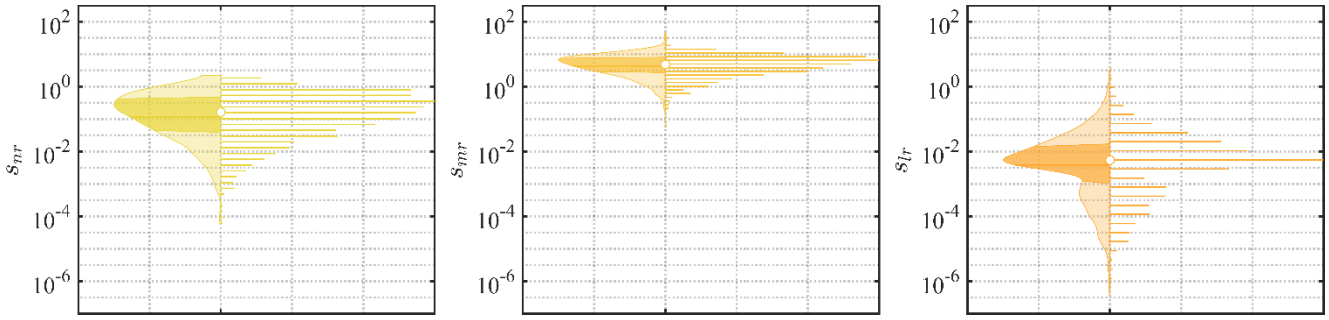

Figure 4. Half-violin plots for the estimated source terms of the different immune cells.

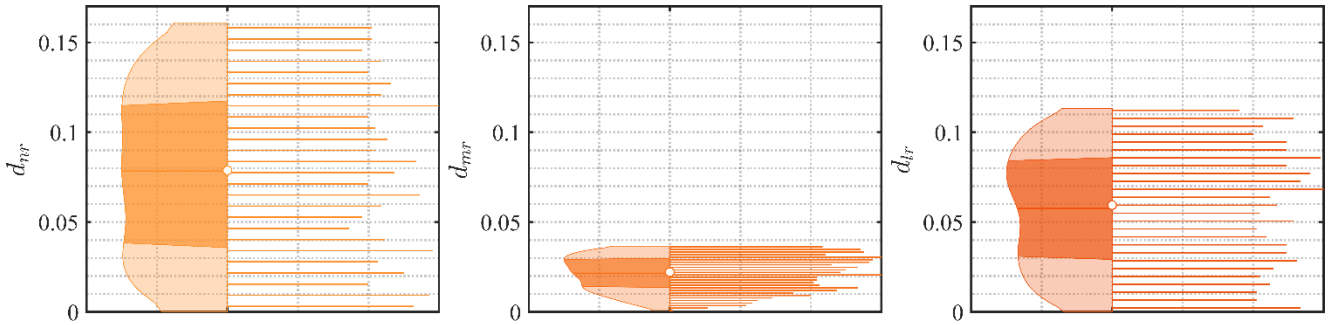

Figure 5. Half-violin plots for the estimated decay rates of resting immune cells.

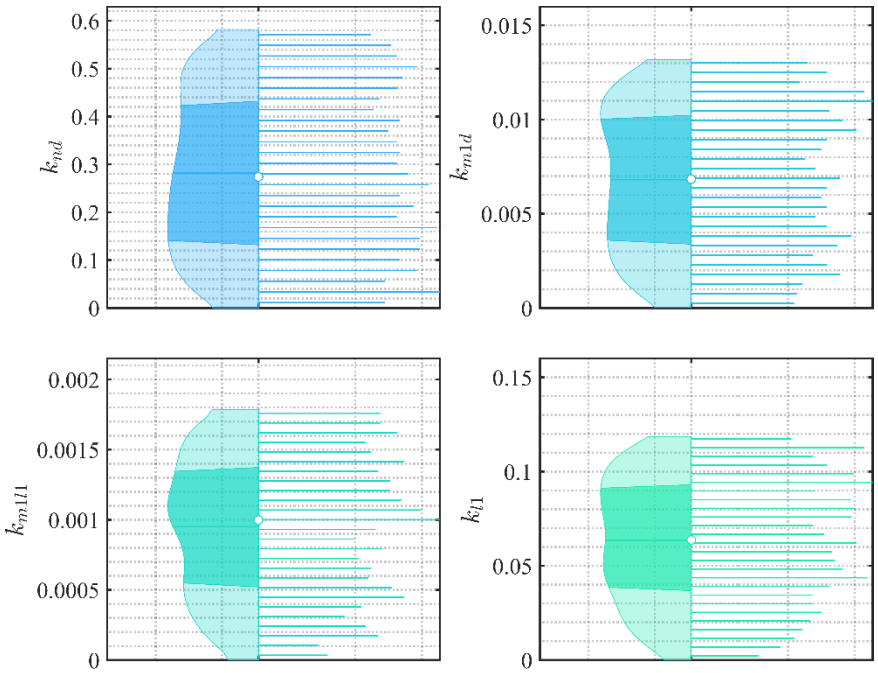

Figure 6. Half-violin plots for the estimated activation parameters of pro-inflammatory immune cells.

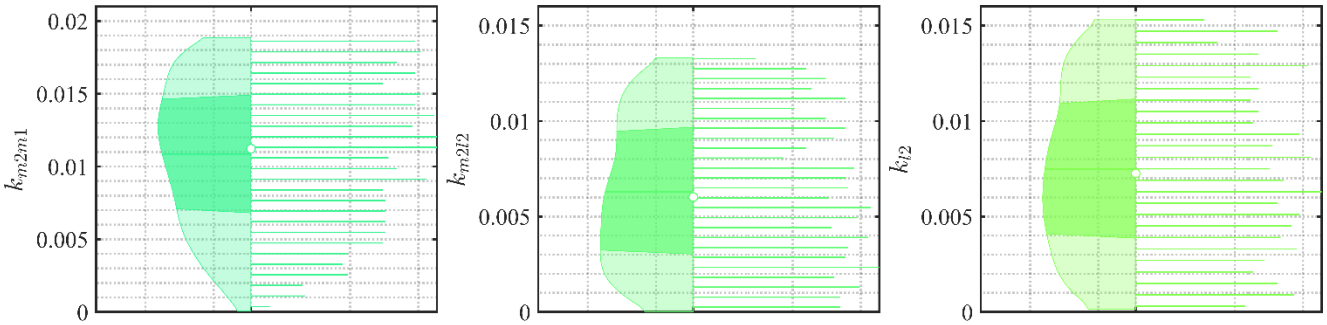

Figure 7. Half-violin plots for the estimated activation parameters of anti-inflammatory immune cells.

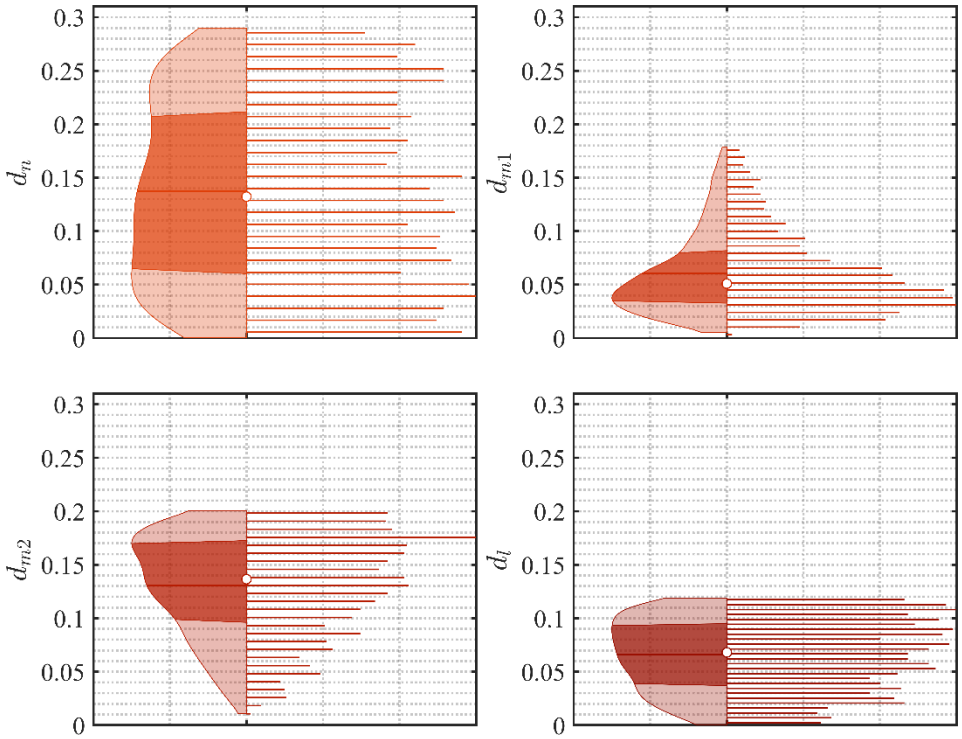

Figure 8. Half-violin plots for the estimated decay rates of activated immune cells.

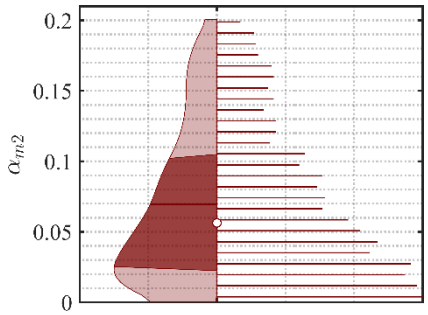

Figure 9. Half-violin plot for the estimated decay rates of resting immune cells.

Figure 9 and Figure 10 display dynamics predicted by the TDPM satisfying Eqns. (1)-(13) for 100 randomly sampled accepted parameter combinations for the two sets of initial conditions representing superficial thickness and partial-superficial thickness burns (see Section 3.3.1). Note the variability in

the predicted immune dynamics for a given initial condition, illustrating the ability of the parameter estimation approach to account for individual heterogeneity.

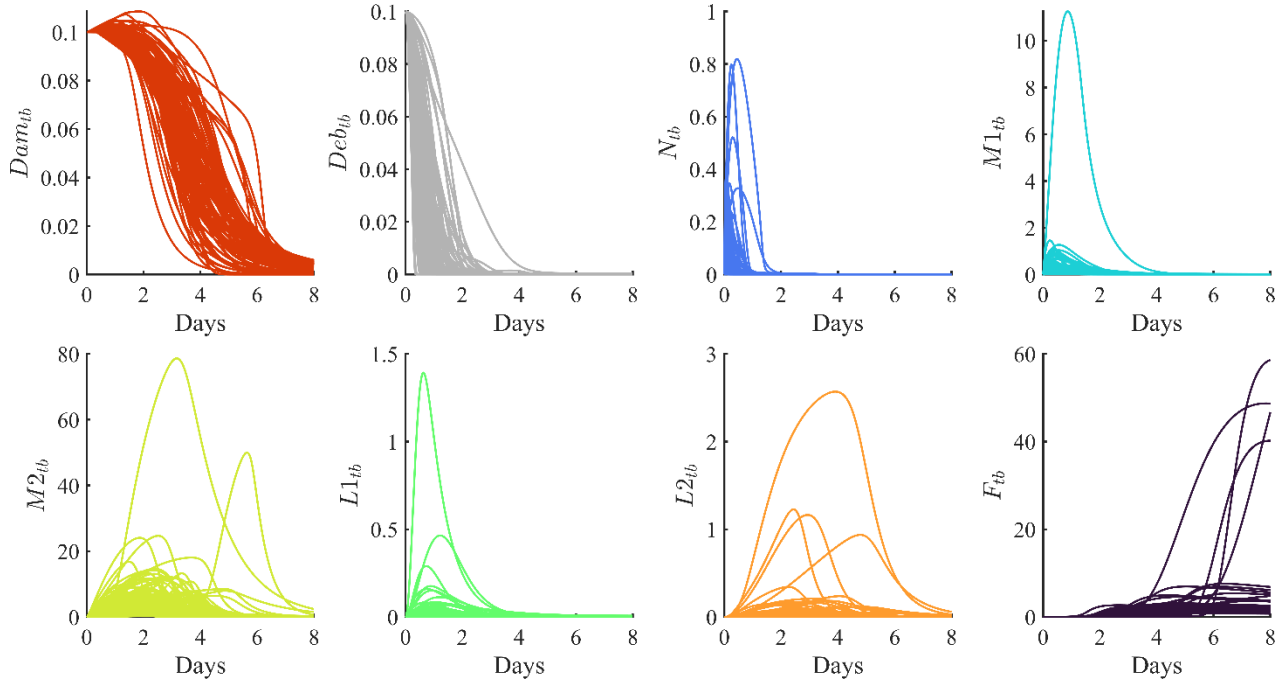

Figure 10. Example dynamics predicted by the TDPM for a superficial thickness injury. The accepted set was randomly sampled 100 times.

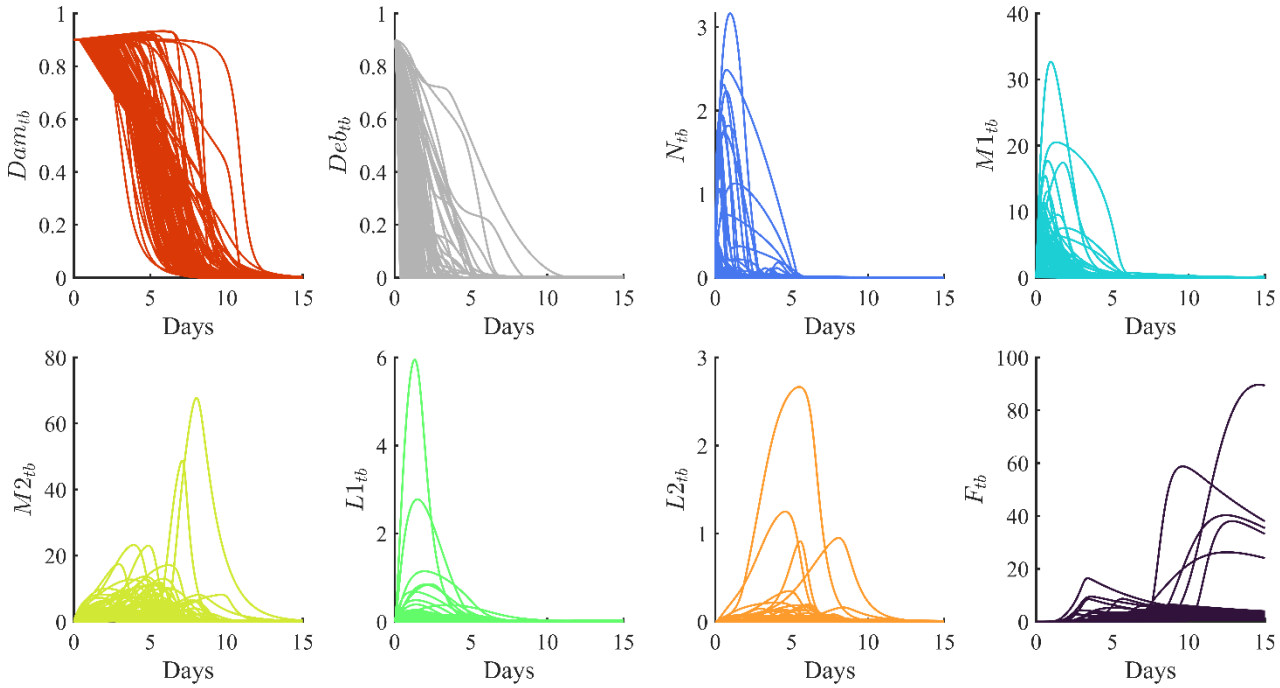

Figure 11. Example dynamics predicted by the TDPM for partial-superficial thickness injury. The accepted set was randomly sampled 100 times.

4.2 Representative Set

The values of the representative set are provided in Table 2. Figure 12 and Figure 13 compare the time series predictions of the representative set against the temporal means used to derive them; recall that the temporal mean is the average at each time point across the predictions of all parameter combinations in the accepted set. Excluding $M1_{tb}$ and F_{tb}, visual inspection suggests similarities in overall shape and the timing of the peaks between the temporal means and the dynamics are satisfactorily predicted by the representative set.

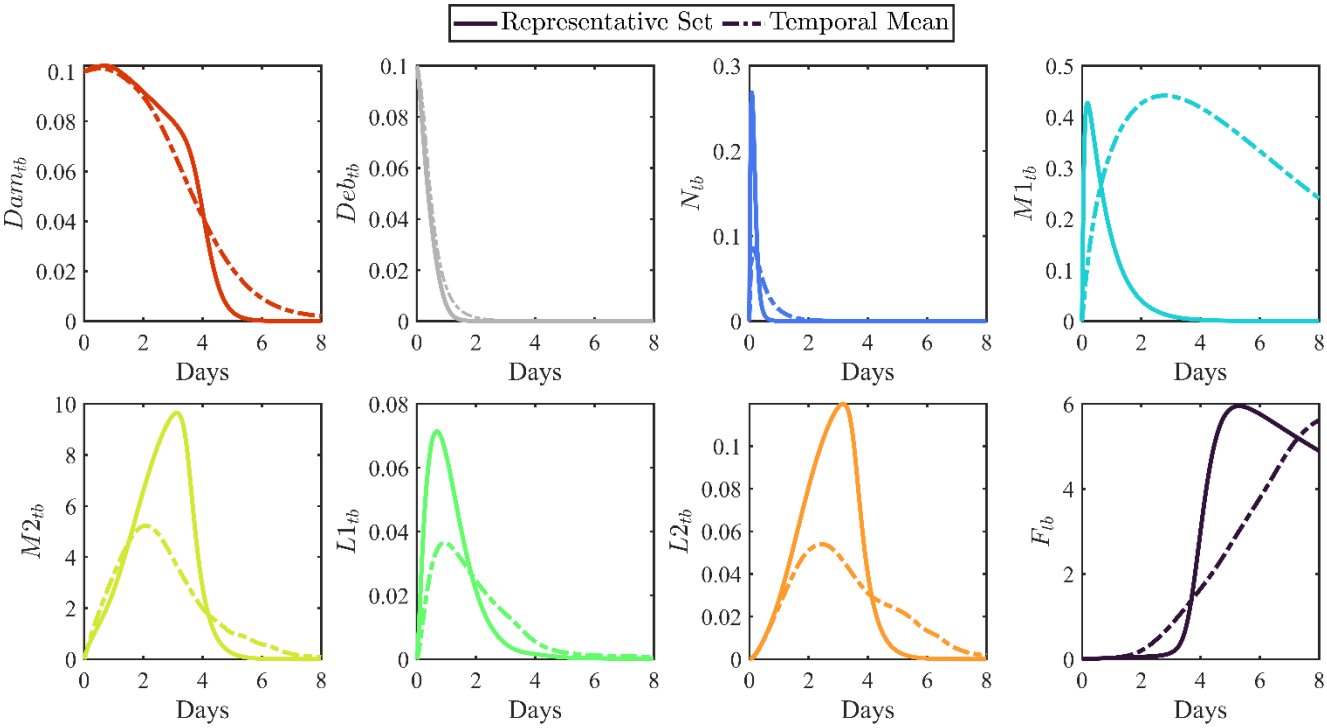

Figure 12. Comparison of dynamics predicted by the representative set (solid lines) and temporal means (dashed lines) for a superficial thickness burn.

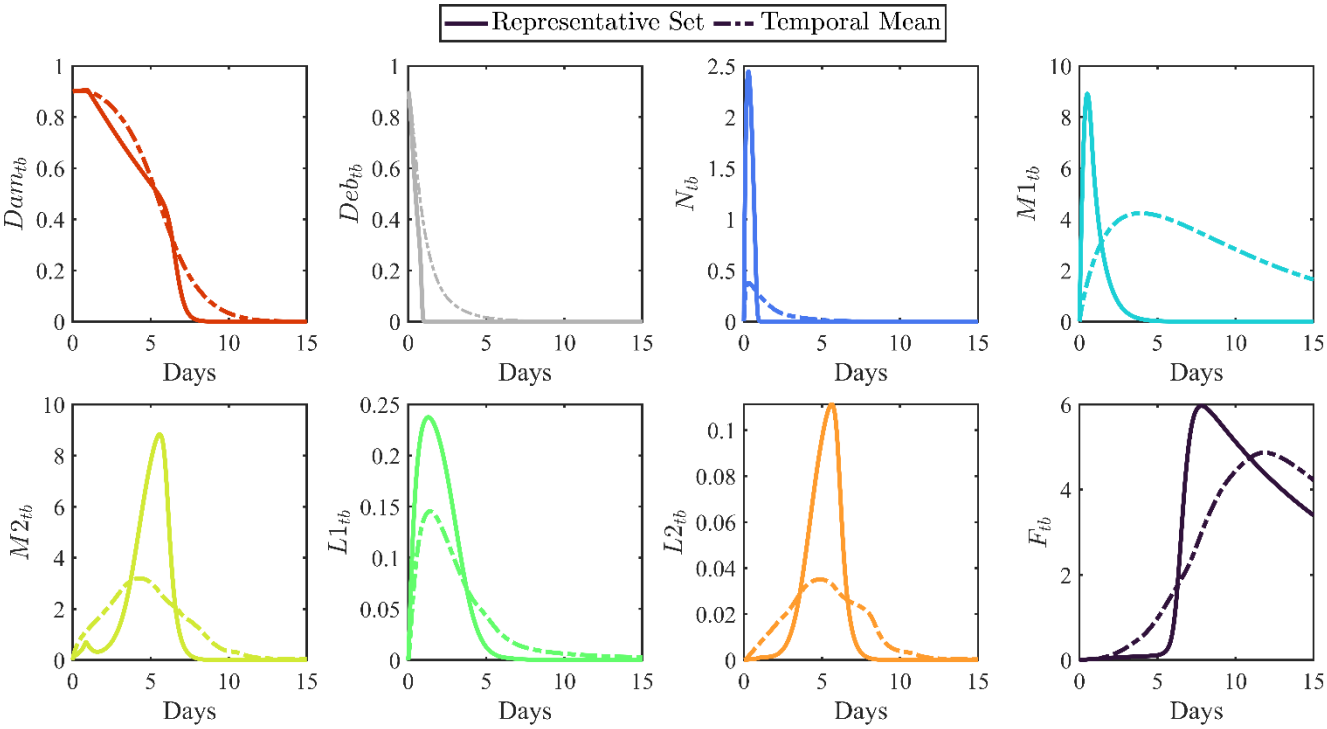

Figure 13. Comparison of dynamics predicted by the representative set (solid lines) and temporal means (dashed lines) for a partial-superficial thickness burn.

R^2 values, which assess the goodness-of-fit between the model time series data predicted by the representative set and temporal means, for each state variable are also reported in Table 5. These values suggest this agreement between the model predictions under the representative set and temporal means is strongest for Dam_{tb}, Deb_{tb}, $M1_{tb}$, $L1_{tb}$, and F_{tb} across both initial conditions. Thus, there remains considerable agreement for $M1_{tb}$ and F_{tb} despite the difference in the timing of the peaks. Similarly, comparison of the curves in Figure 12 and Figure 13 with the values in Table 5, suggests a low R^2 can be primarily attributable to the difference in the magnitude of the peaks as in these cases the overall shape is preserved. The healing times under the representative set for the superficial thickness and partial superficial thickness burns were 4.667 days and 7.833 days, respectively.

Table 5. R^2 values of time series data predicted by representative set for a superficial thickness burn (IC1) and partial superficial-thickness burn (IC2).

INITIAL CONDITIONS	STATE VARIABLE							
	Dam_{tb}	Deb_{tb}	N_{tb}	$M1_{tb}$	$M2_{tb}$	$L1_{tb}$	$L2_{tb}$	F_{tb}
IC1	0.9795	0.9716	0.5368	0.6717	0.7487	0.7521	0.7026	0.7743
IC2	0.9803	0.6441	0.2973	0.7691	0.5724	0.8329	0.5515	0.8377

Next, to provide validation, we demonstrate additional behaviors exhibited by the model as predicted for the representative set. In superficial thermal burns, the pro-inflammatory response peaks around day 1 and begins resolving around day 2 with proliferation commencing around day 5 (Jadhav et al. 2013). An examination of the timing of the peaks for neutrophils, M1 macrophages, and L1 T Lymphocytes in Figure 12 and Figure 13, as predicted by the representative set (solid line), demonstrates the ability of

the model to reproduce this observed behavior. Moreover, the peaks of the anti-inflammatory components, M2 macrophages and L2 T lymphocytes, occur later as desired. The same also holds true for fibroblasts, which begin to grow exponentially slightly before day 5 for both initial conditions. These observations are also visible in Figure 14.

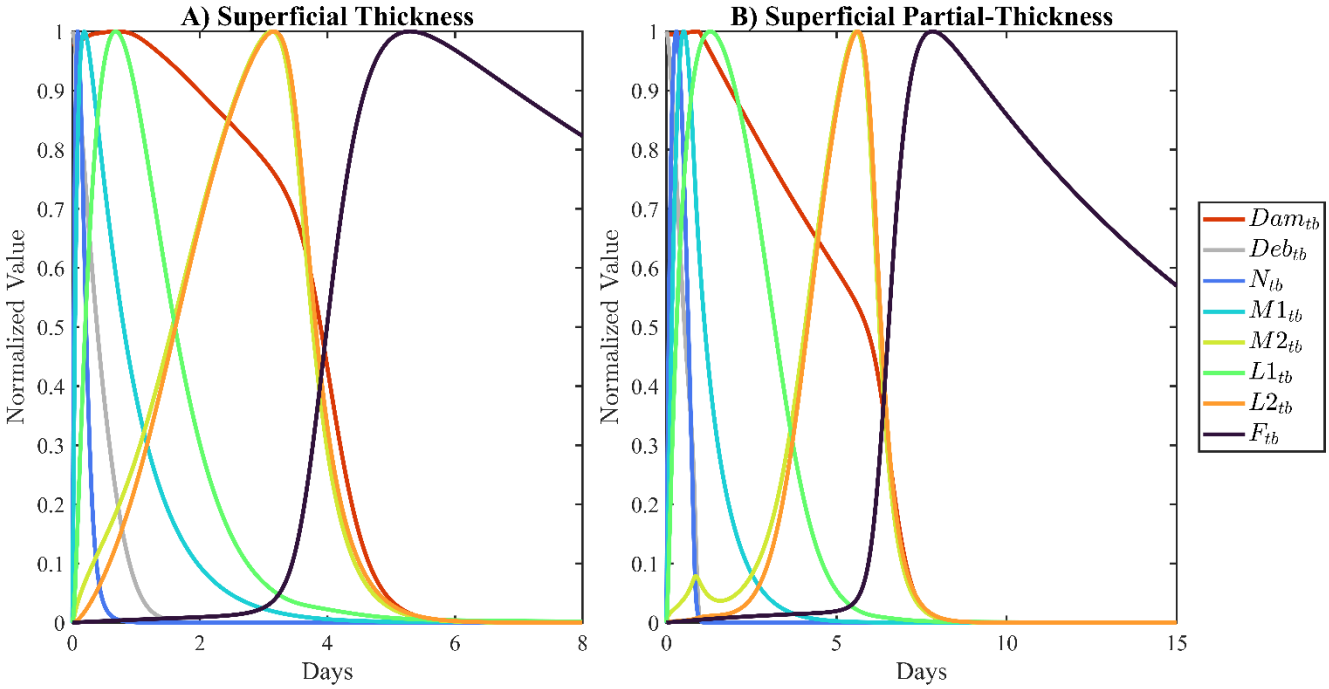

Figure 14. Normalized time-series predictions of the TDPM using the representative set.

More specifically, for superficial thickness thermal burns, neutrophils peak between 3-8 hours following injury (Hensby et al. 1983). For IC1, which represents a superficial thickness injury, neutrophils peak at ~2 hours, demonstrating the capability of the model to come close to capturing the timing of the inflammatory response despite not being explicitly expressed in the acceptability criteria. This rapid, immediate influx of neutrophils has also been observed for minor partial thickness thermal burns, followed by a delayed appearance of macrophages to the wound site (Tyler et al. 2001). For IC2, a superficial partial-thickness burn, neutrophils peak at ~7 hours where M1 and M2 macrophages peak at 12 hours and 5.583 days, respectively. For IC1, the model predicts M1 and M2 macrophages peak at 4.5 hours and 3.125 days, demonstrating the ability to replicate this observed delay in macrophages. In a murine animal model, which used a heated rod that resembled dynamics closer to that of a partial thickness burn with closer to 20% total body surface area, Lateef, et al. found that total macrophages peaked between 1-2 weeks (Lateef et al. 2019), suggesting the precise timing of the macrophage peaks to be highly variable. This variability is to be expected in humans, further reinforcing the parameter estimation approach presented here as the representative set could be recalibrated as more information becomes known.

Other studies have found that early in the inflammatory phase the M1 phenotype dominates the macrophage population at the site of injury, with the same holding true later on, but with M2 being the primary phenotype (Chen et al. 2019). Figure 14 shows the proportion for $M1_{tb}$ and $M2_{tb}$ of the sum $M1_{tb} + M2_{tb}$ as a function of time for the two different superficial burns. In both figures, the local

wound in characterized by M1 immediately following injury; however, their prevalence is considerably diminished shortly after (several hours v. 3 days). In both injuries, the M1 population recovers. It is important to the note that convergence towards a 50-50 split occurs after the healing time when both variables are at or near zero.

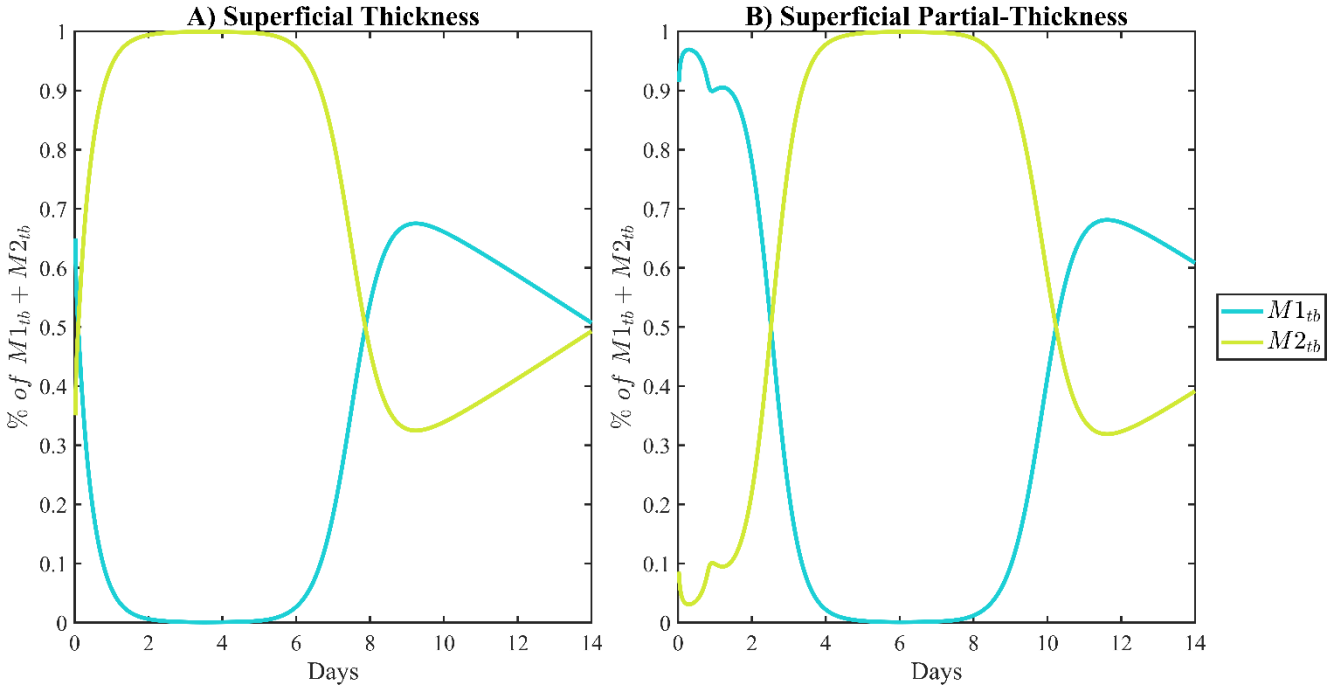

Figure 15. $M1_{tb}$ and $M2_{tb}$ as percentage of $M1_{tb} + M2_{tb}$ versus time predicted by the TDPM using the representative set.

One study using a murine model found that 85% of macrophages exhibited an M1 phenotype one day following injury with this percentage decreasing to 20% by day seven (Daley et al. 2010). Another suggested that while M1 might be the prevalent phenotype much earlier than day one, they represented only 25% of the total macrophage population across all other subsequent time points (Lateef et al. 2019). The variability in the ratio of M1 to M2 macrophages observed in mice highlights that similar variability would be expected for the human response. Here, the representative set represents the parameter combination closest to the average temporal response, and therefore, when validating this set, it is not expected to have perfect correspondence with experimental observations. An advantage afforded by brute-force with LHS is that the representative set could be recalibrated as more information becomes known.

Section 5. Discussion, Future Work, and Potential Impacts

Since they do not come with increased risk of mortality, superficial thermal injuries lack the attention afforded to more severe burns. However, to advance HENRE's capabilities for dynamically predicting performance degradation, these non-life threatening injuries are of the utmost relevance as they are associated with varying degrees of pain (Vigani and Culler 2017; Lateef et al. 2019). For thermal burns in military personnel, the face, neck, and hands are also the predominant injury location (Reeves 2018). By the Rule of Nines, the percent of total body surface area injured would be at most 13-19% (Wang 2014; Reeves 2018). Moreover, in the non-idealized (e.g., urban environment or where soldiers are in heavily armored vehicles), various structures will provide a considerable degree of shielding against thermal radiation, and this protection can also be enhanced by the uniforms of military personnel (Reeves 2018). In addition, all burns are of interest with respect to combined injury due the potential for synergistic effects.

Estimates of 27 critical parameters of a TDPM for superficial thermal burns were obtained via brute-force with LHS. This method was selected due to the lack of a singular dataset that aligned with the model, i.e., local immune cell and fibroblast populations. A total of 1,298 parameter combinations satisfied the acceptability criteria, which reflected observed wound healing trends for superficial injuries. This collection of parameter sets can be viewed as a characteristic population of individuals with heterogeneous wound healing responses following superficial injury (Cooper et al. 2015). A representative set was then extracted from theses accepted parameter combinations to obtain single point-wise estimates for each parameter. It was shown that the representative set was also capable of reproducing dynamics not imposed during the parameter estimation process. With the parameterized TDPM of superficial injury, HENRE's capabilities could be expanded to include time-to-healing, a potential surrogate metric for return-to-duty.

Future work will first focus on linking inputs characterizing the thermal insult environment to initial conditions of the TDPM; noting that the latter captures the level of injury. Currently, thermal models within HENRE do not use specific levels of injury relating precisely to an individual's exposure to a NUDET thermal insult environment, such as thermal radiation. Rather, the models accept a range of initial values corresponding to thermal fluence (energy/cm^2) or percent total body surface area (%TBSA) with second-degree burns. The authors believe that damage-associated molecular patterns, also referred to as DAMPS, are the key to constructing this initial condition mapping. Secondary work will then try to connect the time series data predicted by the model under the representative set or acceptable set (as determined by the outcome of interest) to performance degradation or other clinical effects. This end-to-end framework serves as a foundational structure for expanding into injuries resulting from exposure to combined insults.

Section 6. References

Abazari M, Ghaffari A, Rashidzadeh H, Badeleh SM, Maleki Y. A systematic review on classification, identification, and healing process of burn wound healing. Int J Low Extrem Wounds 1–13; 2020.

Bechtold B. Violin Plots for Matlab, Github Project. 2016.

Blower SM, Dowlatabadi H. Sensitivity and uncertainty analysis of complex models of disease transmission: An HIV model, as an example. Int Stat Rev 62:229; 1994.

Chen L, Wang J, Li S, Yu Z, Liu B, Song B, Su Y. The clinical dynamic changes of macrophage phenotype and function in different stages of human wound healing and hypertrophic scar formation. Int Wound J 16:360–369; 2019.

Cooper RL, Segal RA, Diegelmann RF, Reynolds AM. Modeling the effects of systemic mediators on the inflammatory phase of wound healing. J Theor Biol 367:86–99; 2015.

Creel A, Jennings R, Reynolds A. Sensitivity Analysis for a Time-Dependent Physiological Model of Superficial Thermal Burns. DTRA-TR-21-063 R1, Defense Threat Reduction Agency, Fort Belvoir, VA; 2022.

Daley JM, Brancato SK, Thomay AA, Reichner JS, Albina JE. The phenotype of murine wound macrophages. J Leukoc Biol 87:59–67; 2010.

Diegelmann RF, Evans MC. Wound Healing: An overview of acute, fibrotic and delayed healing. Front Biosci 9:283–289; 2004.

Evers LH, Bhavsar D, Mailänder P. The biology of burn injury. Exp Dermatol 19:777–783; 2010.

Finnerty CC, Jeschke MG, Branski LK, Barret JP, Dziewulski P, Herndon DN. Hypertrophic scarring: the greatest unmet challenge after burn injury. Lancet 388:1427–1436; 2016.

Goldberg SR, Diegelmann RF. Wound healing primer. Surg Clin North Am 90:1133–1146; 2010.

Hensby CN, Barr RM, Black AK, Mallet AI, Greaves MW. Histologic changes associated with ultraviolet A-induced erythema in normal human skin. J Am Acad Dermatol 9:213–219; 1983.

Hettiaratchy S, Dziewulski P. ABC of Burns: Pathophysiology and types of burns. BMJ 328:1427–1429; 2004.

Jadhav SS, Sharma N, Meeks CJ, Mordwinkin NM, Espinoza TB, Roda NR, Dizerega GS, Hill CK, Louie SG, Rodgers KE. Effects of combined radiation and burn injury on the rennin-angiotensin system. Wound Repair Regen 21:131–140; 2013.

Jennings R, Creel A, Reynolds A. A Time-Dependent Physiological Model of Innate and Adaptive Immune Responses Activated by Superficial Thermal Burns. DTRA-TR-21-032 R1, Defense Threat Reduction Agency, Fort Belvoir, VA; 2022.

Jeschke MG, van Baar ME, Choudhry MA, Chung KK, Gibran NS, Logsetty S. Burn injury. Nat Rev Dis Prim 6; 2020.

Lateef Z, Stuart G, Jones N, Mercer A, Fleming S, Wise L. The cutaneous inflammatory response to thermal burn injury in a murine model. Int J Mol Sci 20; 2019.

Marino S, Hogue IB, Ray CJ, Kirschner DE. A methodology for performing global uncertainty and sensitivity analysis in systems biology. J Theor Biol 254:178–196; 2008.

McKay MD, Beckman RJ, Conover WJ. A comparison of three methods for selecting values of input variables in the analysis of output from a computer code. Technometrics 21:239–245; 1979.

Minucci S, Heise RL, Valentine MS, Kamga Gninzeko FJ, Reynolds AM. Mathematical modeling of ventilator-induced lung inflammation. J Theor Biol 526; 2021.

Peng D, Huang W, Ai S, Wang S. Clinical significance of leukocyte infiltrative response in deep wound of patients with major burns. Burns 32:946–950; 2006.

Reeves G. Chapter 14: Effects on Personnel (Revision 1). In: EM-1: Capabilities of Nuclear Weapons. DTRA-EM-1-CH-14 (R1), Defense Threat Reduction Agency, Fort Belvoir, VA; 2018.

Schultz GS, Chin GA, Moldawer L, Diegelmann RF. Principles of Wound Healing. In: Fitridge R and Thompson MM, eds. Mechanisms of Vascular Disease: A Reference Book for Vascular Specialists. University of Adelaide Press; 2011:423–449.

Strudwick XL, Cowin AJ. The role of the inflammatory response in burn injury. In: Hot Topics in Burn Injuries. InTech; 2018.

Tyler M, Watts A, Perry M, Roberts A, McGrouther D. Dermal cellular inflammation in burns. an insight into the function of dermal microvascular anatomy. Burns 27:433–438; 2001.

Vigani A, Culler CA. Systemic and local management of burn wounds. Vet Clin North Am - Small Anim Pract 47:1149–1163; 2017.

Wang C. Assessment and Physiology of Burns. In: Anesthesia for Trauma: New Evidence and New Challenges. Springer, New York, NY; 2014:271–289.

MATLAB 2020b. The MathWorks, Inc., Natick, MA, U.S.A.; 2020.

Appendix A. Abbreviations and Acronyms

ACRONYM	MEANING
ARA	Applied Research Associates, Inc.
DAMPS	Damage-associated molecular patterns
DTRA	Defense Threat Reduction Agency
eFAST	Extended Fourier Amplitude Sensitivity Test
HENRE	Health Effects from Nuclear Radiological Environments
LHS	Latin-Hypercube Sampling
NUDET	Nuclear Detonation
ODE	Ordinary Differential Equation
TDPM	Time-Dependent Physiological Model